ADVANCED FUNCTIONAL MATERIALS
www.afm-journal.de

Accelerated Kinetics of Desolvation and Redox Transformation Enabled by MOF Sieving for High-Loading Mg-S Battery

Qinghua Guan, Quan Zhuang, Wenlong Xu, Yongzheng Zhang, Shuang Cheng, Jing Zhang, Meinan Liu, Hongzhen Lin, and Jian Wang**

Magnesium-sulfur (Mg-S) batteries have attracted growing interest as a promising candidate of post-lithium-ion battery systems due to their high energy density, natural abundance of Mg and S, and superior safety. However, they are severely inhibited by the sluggish electrochemical kinetics of interfacial Mg^{2+} desolvation and successive sulfur redox species conversions, leading to dissatisfactory "shuttling effect". Herein, a strategy of combining porous sieve desolvation and molecular electrocatalysis is proposed to dissociate Mg^{2+}-solvents structure, stimulate free Mg^{2+} diffusion, and further improve the kinetics of sulfur redox conversion. As a protocol, the metal-organic frameworks (MOF) of representative MIL-101(Cr) with pore structure is capable of sieving larger $Mg(solvents)_x^{2+}$ cluster to release free Mg^{2+} to react with sulfur species, and also the Lewis acid site of central Cr(III) can effectively adsorb and transform polysulfides, as thoroughly revealed by experimental and in situ/ex situ characterizations. Consequently, the as-fabricated Mg-S batteries employed with MIL-101(Cr)-decorated separator can deliver the capacity of 974 mA h g^{-1} after 250 cycles, and exhibit a high-rate performance of 694 mA h g^{-1} at 2 C. Impressively, the high-mass-loading cell of 6.4 mg cm^{-2} stabilizes for more than 60 cycles, demonstrating the polar MOF with pore sieving effect for practical application of Mg-S batteries.

1. Introduction

In pursuit of developing ecological, large-scale, high-efficiency energy storage systems,[1] magnesium-sulfur (Mg-S) batteries have become one of the most attractive battery systems due to superior volume energy density (3221 Wh L^{-1}), high safety, low cost of abundant resources.[2] Currently, the development of Mg-S batteries is still in the preliminary stage and there are still some problems that needs to be solved urgently: 1) Screening and designing the compatible electrolyte system for Mg-S batteries;[3] 2) Activating the Mg passivation layer to accelerate magnesium ions diffusion;[4] 3) Accelerating the dissociation and conversion kinetics by decreasing high barriers of "solid-liquid-solid" multistep aiming at intrinsic non-conductivity of sulfur, large volume changes, and severe polysulfide shuttling.[5]

To address the problems of sulfur cathodes in Mg-S batteries, current efforts

Q. Guan, S. Cheng, H. Lin
School of Nano-Tech and Nano-Bionics
University of Science and Technology of China
Hefei 230026, China
E-mail: hzlin2010@sinano.ac.cn

Q. Guan, S. Cheng, H. Lin, J. Wang
i-Lab & CAS Key Laboratory of Nanophotonic Materials and Devices
Suzhou Institute of Nano-Tech and Nano-Bionics
Chinese Academy of Sciences
Suzhou 215123, China
E-mail: wangjian2014@sinano.ac.cn, jian.wang@kit.edu

J. Wang
Helmholtz Institute Ulm (HIU)
D89081 Ulm, Germany

The ORCID identification number(s) for the author(s) of this article can be found under https://doi.org/10.1002/adfm.202506397

DOI: 10.1002/adfm.202506397

J. Wang
Karlsruhe Institute of Technology (KIT)
D76021 Karlsruhe, Germany

Q. Zhuang
Inner Mongolia Key Laboratory of Carbon Nanomaterials
Nano Innovation Institute (NII)
College of Chemistry and Materials Science
Inner Mongolia Minzu University
Tongliao 028000, China

W. Xu
Inszitute of Agricultural Resources and Environment
Jiangsu Academy of Agricultural Sciences
Nanjing 210014, China

J. Zhang
School of Materials Science and Engineering
Xi'an University of Technology
Xi'an 710048, China

mainly focused on looking for suitable electrolytes in match with magnesium anode and sulfur cathodes;[3c,6] constructing conductive carbon/sulfur composites with excellent structure to achieve high conductivity and adapt to the volume change in the sulfur conversion process;[7] designing and introducing active sites to inhibit the shuttle effect of soluble magnesium polysulfides (MgPSs), adsorb MgPSs physically or chemically and further promote MgPSs transformation.[8] However, whatever electrolytes and sulfur systems are, the electrochemical performance of batteries are far from practical expectation due to the high transformation barriers among sulfur species.[9] Meanwhile, as known, the Mg^{2+}-solvents clusters are the main charge carriers in the electrolyte or at the interface, and less attention or strategies centered on the status or roles of Mg^{2+} in the inner Helmholtz plane layer on the effects of polysulfide conversions.[10] In the current electrolyte systems, the Mg^{2+} is easy to coordinate with solvents to form large $Mg(solvents)_x^{2+}$ structures with huge steric immobilization, which will render slow diffusion kinetics and affect the successive redox performance.[3c,11] The most common strategy for regulating the dissolved structure is to optimize the electrolyte compositions of adding various additives such as electrolyte diluent.[12] Different from electrolyte engineering, our group also explored another strategy of adopting interfacial catalytic desolvation method to strengthen the Li/Zn ion dissociation process.[13] Thus, the ideal solution to accelerate the dissociation of $Mg(solvents)_x^{2+}$ structure is constructing interfacial catalytic sites to form more isolated Mg^{2+}, promoting the kinetics of sulfur redox reaction.

As known, metal-organic frameworks (MOF) are famous for their porosity and structural adjustability, which are widely used in electrochemical fields.[14] For example, Zhou et al. developed a MOF modified electrolyte, in which solvent molecules can be screened for free Li^+ by MOF with suitable pore size.[15] Grafting conductive carbon on the MOFs can also serve as the sieving skeleton for realizing increased numbers of Li^+ flux with enhanced transport for fast redox conversion kinetics.[13d] However, most reports mainly utilize the pore morphology to sieve larger size cluster and there are seldom reports focused on the effect of metal center site. Among the various metal centers, the Lewis acidic Cr(III) center shows the stronger capability in polysulfide adsorption through Lewis acid-based interaction.[16] Therefore, it is of significance to investigate the Lewis acid-based MOFs on the kinetics improvement toward Mg^{2+} dissociation and further sulfur redox conversions.

M. Liu
State Key Laboratory of Featured Metal Materials and Life-cycle Safety for Composite Structures
Guangxi Key Laboratory of Processing for Non-Ferrous Metals and Featured Materials
School of Resources
Environment and Materials
Guangxi University
Nanning 530004, China
Y. Zhang
State Key Laboratory of Chemical Engineering
East China University of Science and Technology
Shanghai 200237, China

Herein, MIL-101 (Cr) with Lewis acid center is selected as the porous MOF material, to fabricate a modified glass fiber separator coating (MIL101-GF) through a simple vacuum filtration method. The MIL101-GF is applied to the side of the cathode and played the role of upper fluid collection on the sulfur cathode. The multistage pore structure of MIL-101 (Cr) can effectively accelerate the dissociation of $Mg(solvents)_x^{2+}$, release a large amount of free Mg^{2+}, which subsequently participate in the transformation reaction of MgPSs. Moreover, due to the presence of Lewis acid Cr(III) centers, MgPSs can be adsorbed and quickly converted. The as-fabricated Mg-S batteries employed with MIL101-GF separator could maintain a high capacity of 974 mA h g^{-1} after 250 cycles at 0.5 C, also operate stably at 2 C with high-rate performance of 694 mA h g^{-1}. More excitedly, the cell with MIL101-GF demonstrated stable performance over 60 cycles even at a high sulfur loading of 6.4 mg cm^{-2}. It is proved that MIL101-GF coating can effectively accelerate the dissociation of $Mg(solvents)_x^{2+}$, inhibit the transfer of MgS_x and promote the transformation of polysulfide, effectively improve the electrochemical performance of Mg-S batteries, and prolong its working life.

2. Results and Discussion

The density functional theory (DFT) calculations were conducted to gain insights into the decoupled transportation of $MgCl_2(THF)_2$ into THF and $MgCl_2$·THF in liquid electrolyte and on MIL-101(Cr) substrate.[11] As shown in **Figure 1A,B**, the desolvation barrier of $MgCl_2(THF)_2$ on MIL-101(Cr) is 0.75 eV, lower than the case in liquid electrolyte. Therefore, MIL-101(Cr) is more conducive to decoupling $MgCl_2(THF)_2$ and thereby easily dissociating to form free Mg^{2+}. Then the interactions and catalytic functions of MIL-101(Cr) in sulfur species adsorption and decomposition were displayed in Figure 1C and Figures S1 and S2 (Supporting Information).[8d,17] All structures and free energies of the S_8 and various MgS_x (x = 1, 2, 4, 6, 8) species were optimized on MIL-101(Cr) substrate and carbon structure. As shown in Figure 1D, the adsorption energies of MgS_x (x = 1, 2, 4, 6, 8) species on the MIL-101(Cr) substrate are higher than the case on carbon structure. For example, the MIL-101(Cr) displays the improved binding energy of 2.25 eV to MgS_6, ≈3.2 times higher than that on carbon structure. It is worth noting that S_8 exists as a cyclic molecule with a symmetric structure and uniform electron cloud distribution, lacking polarity or active sites, which hinders its ability to form strong chemical bonds with MIL-101(Cr). On the other hand, MgS_x possesses relatively high polarity and hence shows enhanced adsorption affinity to the porous MOF of MIL-101(Cr) containing Lewis acidic metal sites through Cr-S_x^{2-} interactions. The nonpolar surface of carbon materials favors hydrophobic attractions to the S_8 molecules, while exhibits low affinity toward polar species such as MgS_x. A high adsorption energy of MIL-101(Cr) for MgS_x can suppress polysulfide dissolution and shuttling and enhance the catalytic conversion efficiency, thereby improving cycling stability, whereas the preferential adsorption of S_8 on the carbon surface facilitates the redeposition of S_8 onto the electron-conductive network for electrochemical reduction in the following cycle. Admittedly, there is a risk that the catalytic sites in MIL-101(Cr) would be covered by non-soluble MgS_2 and MgS deposits. The soluble long chain MgPSs can serve as redox mediators for activating the MgS_2 and

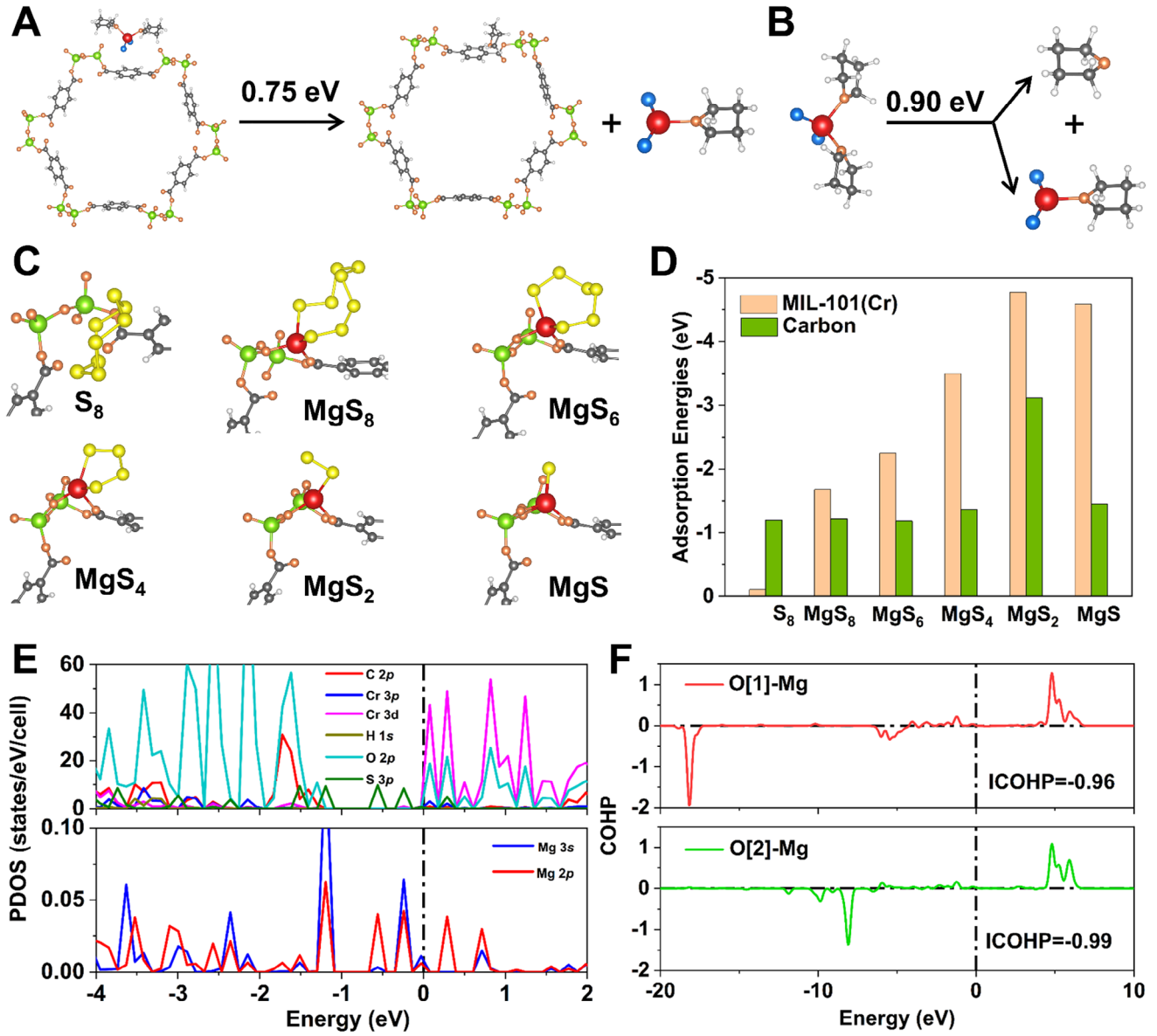

Figure 1. Systematic self-tandem catalysis of MIL101-GF revealed by theoretical simulations. Desolvation barrier of $MgCl_2(THF)_2$ into THF and $MgCl_2$·THF A) on MIL-101(Cr) substrate and B) in liquid electrolyte. C) The adsorption configurations and adsorption energies of MgS, MgS_2, MgS_4, MgS_6, MgS_8, and S_8 on MIL-101(Cr) catalysts. D) Comparison of adsorption binding energies between sulfur species and various matrix. E) The projected density of states (PDOS) for the adsorbed configuration of MgS_6 on MIL-101(Cr) substrate. F) COHP for the interactions between O and Mg atoms for MgS_6 adsorption on MIL-101(Cr) substrate. The negative and positive COHP denote bonding and antibonding interactions.

MgS through comproportionation reaction and thus re-expose the catalytic sites. The interactions can be supported by the projected density of states (PDOS) and crystal orbital Hamilton population (COHP) analyses (Figure 1E,F; Figures S3 and S4, Supporting Information).[18] For MIL-101(Cr), the hybridizations between the electronic orbitals of O and Mg atoms are apparent, which is consistent with the COHP results that the electrons fully occupy the bonding states for the O—Mg bonds, suggesting strong interactions. As for carbon structure, the anti-bonding states emerge below the Fermi level, suggesting the relative weak binding between the C-Mg atoms. The bonding strength can be quantitively expressed by the integral COHP (ICOHP), the larger absolute value of ICOHP means a stronger binding. For MgS_6 adsorption on MIL-101(Cr), values of ICOHP corresponding to the two O—Mg bonds are −0.96 and −0.99 (Figure 1F), significantly superior to the C—Mg (ICOHP = −0.14) bond in C-MgS_6 (Figure S4, Supporting Information).

As shown in **Figure 2**A, we selected MIL-101 (Cr) as the material to accelerate the dissociation of $Mg(solvents)_x^{2+}$, provide a site for anchoring MgPSs and catalyzing their transformation. It was fully mixed and dispersed in ethanol with nitrogen-doped graphene (NG), and then uniformly deposited on the separator surface by vacuum filtration method (MIL101-GF), corresponding to the sulfur cathode.[8b] MIL-101 (Cr) promotes the

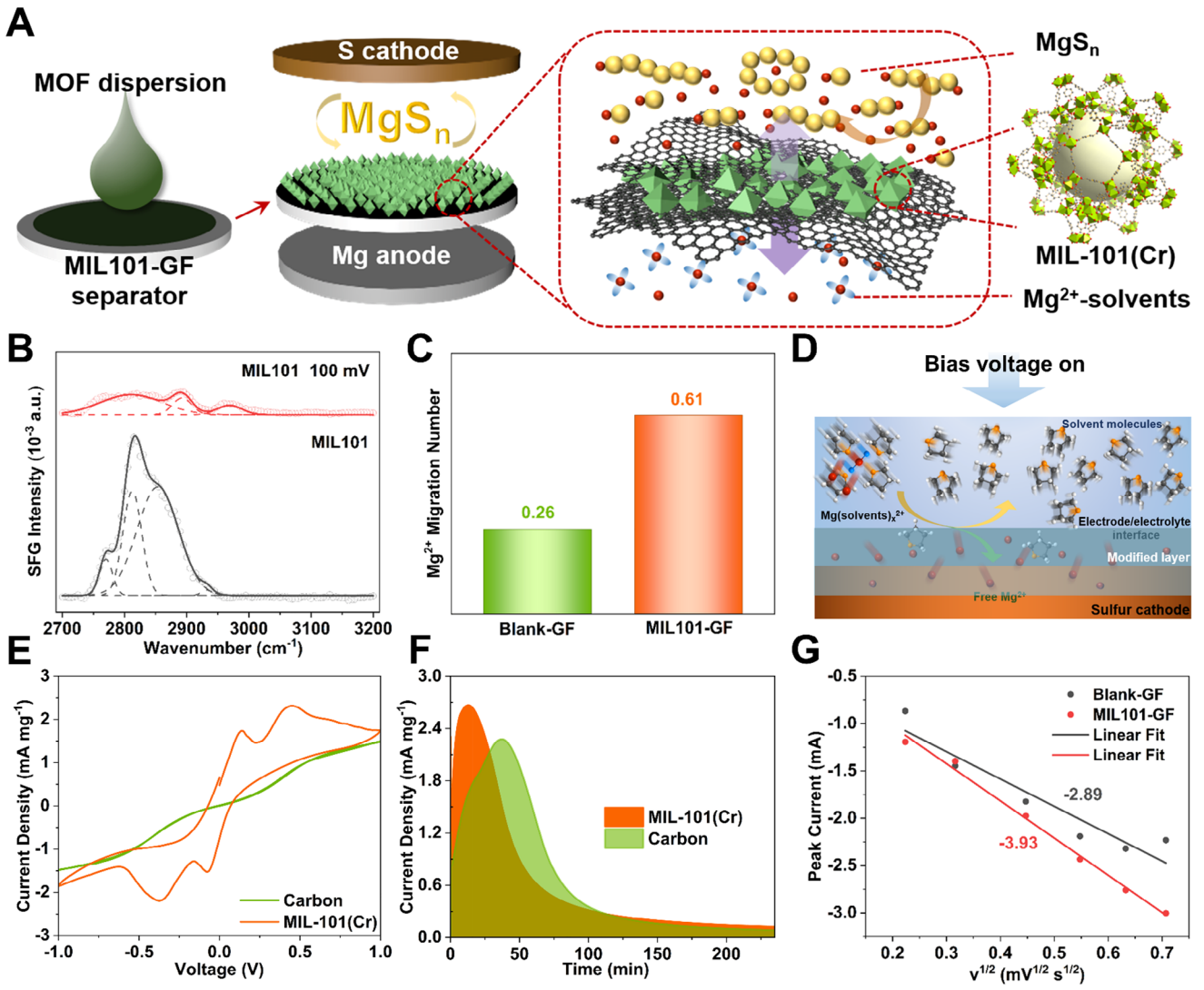

Figure 2. Experimental of interfacial desolvation and sulfur species kinetics catalyzed by MIL101-GF. A) Schematic diagram of preparation and structure of MIL101-GF. B) The SFG spectra of different adsorption states of $Mg(solvents)_x^{2+}$-structure in $MgCl_2$-LiCl/THF electrolyte. C) Magnesium ion migration number for Blank-GF and MIL101-GF. D) The molecular states of the $Mg(solvents)_x^{2+}$-structure in the MIL101-GF electrode/electrolyte interface after turning bias voltage on. E) Comparisons of MgPSs conversions in symmetric cell based on the Carbon and MIL-101(Cr), respectively. F) Comparison of MgS precipitation kinetics on the surface between Carbon and MIL-101(Cr) at a constant potential of 0.7 V, corresponding to a liquid/solid phase transition. G) The slope about square root of scan rate versus peak current.

dissociation of $Mg(solvents)_x^{2+}$ structure to release a large amount of free Mg^{2+}, effectively limits the shuttle of MgPSs through strong physical/chemical adsorption, and the continuous conductive layer conducts electrons rapidly, efficiently transforming MgPSs at the electrode/electrolyte interface with its unique hierarchical porous structure and abundant active sites. The morphology and structure of MIL-101 (Cr) powder are briefly characterized (Figure S5, Supporting Information). MIL-101 (Cr) has a clear octahedral particle structure seen from the scanning electron microscopy (SEM) image, and the energy-dispersive spectroscopy (EDS) mapping results the elements are evenly distributed in MIL-101 (Cr) (Figure S5C, Supporting Information). The X-ray powder diffraction (XRD) patterns in Figure S5D (Supporting Information) clearly demonstrate the characteristic peaks of the MIL-101 (Cr) powder are consistent with those of the theoretical calculation results. MIL-101 (Cr) has a hierarchical channel structure with two apertures: mesoporous cages and microporous windows.[19] The results of N_2 adsorption–desorption isotherms show that it is mainly microporous pores, and there are also mesoporous pores (Figure S6, Supporting Information). The thermogravimetric analysis (TGA) test result of MIL-101(Cr) is shown in Figure S7 (Supporting Information), which could be seen that the weight loss was low below 150 °C, so there is no significant influence on the assembled batteries under normal room temperature experimental conditions.

For the obtained MIL101-GF, we also characterized its morphology and structure, and verified that MIL-101 (Cr) could still retain its original structure and basic properties on the separator

after a series of treatments. As shown in Figure S8A,B (Supporting Information), MIL-101 (Cr) particles were evenly dispersed with NG sheets, and MIL-101 (Cr) particles still had a clear octahedral structure, indicating that the structure of MIL-101 (Cr) particles was not destroyed during the ultrasonic dispersion and extraction filtration process, which proved that MIL-101 (Cr) has excellent stability. Figure S8 (Supporting Information) showed that carbon and nitrogen elements were evenly distributed, which meant that NG sheets were evenly distributed and completely covered the surface of the separator, forming a continuous and uniform modification layer. The XRD diffraction peak of MIL101-GF is consistent with that of MIL-101 (Cr) powder (Figure S8C, Supporting Information), which proves that the structural characteristics of MIL-101 (Cr) hardly change in the process of ultrasonic dispersion and filtration drying, and the bulged peak near 20° corresponds to the presence of carbon, which is also due to the incorporation of NG.[20] As shown in Figure S8 (Supporting Information), the MIL-101(Cr) modified layer was uniformly and tightly deposited on one side of the separator without passing through the separator. The modified separator was repeatedly folded, and no delamination or material fall occurred after restoration (Figure S9, Supporting Information), indicating that the MIL101-GF modified layer had good mechanical stability and flexibility. To test the thermal stability of the coating, a piece of MOF-modified separator on a heating plate, keeping the temperature at 50, 100, 150, and 200 °C respectively for 10 min before bending and recovering it. As can be seen from Figure S10 (Supporting Information), the MIL101-GF did not have any cracks or wrinkles after the above processing. As shown in Figures S11 and S12 (Supporting Information), the contact angle of the electrolyte on the MIL101-modified separator is small, confirming that MIL-101(Cr) introduction effectively enhances electrolyte wettability. Both CV and LSV results indicate that the MIL101-GF could maintain stability during the test (Figures S13 and S14, Supporting Information).

The porous structure on MIL101-GF promotes the dissolution of the $Mg(solvents)_x^{2+}$ structure, allowing more free Mg^{2+} to reach the electrode/electrolyte interface through the MIL-101 (Cr) modified coating, and further participate in the subsequent redox conversion of MgPSs. The interfacial arrangement of cations/anions can be described by the double-layer model of the inner Helmholtz layer and the outer diffusion layer.[21] The ions in the inner layer can exist in the form of solvated, partially solvated, or free ions without any solvent shell, and the ions in the outer layer are dominated by solvated ions.[22] In situ interface-sensitive sum frequency generation (SFG) spectroscopy (see Figure S15, Supporting Information for setup configuration) was applied to monitor the solvation/desolvation process at the interface by detecting the variation of interfacial solvent molecules at open circuit potential or under a certain bias voltage (Figure 2B). The C-H stretching vibration of tetrahydrofuran (THF) at the electrode/electrolyte interface in the range of 2700–3000 cm^{-1} was studied by SFG spectroscopy with ssp polarized. Without bias voltage, THF-related SFG resonances at the electrode/electrolyte interface can be clearly divided into two groups: 2812 and 2855 cm^{-1} have similar characteristics to pure THF and can be attributed to free solvent molecules, while 2770 and 2930 cm^{-1} correspond to THF in the ionic solvated shell.[11a] It can be seen from Figure 2B that the SFG strength is significantly reduced and the solvated shell THF signal almost disappears when a bias voltage of 100 mV is applied, while the retention peak (2812 cm^{-1}) should be allocated to free, non-specifically adsorbed THF molecules. Two characteristic peaks observed at 2890 and 2960 cm^{-1} can be attributed to other FR patterns of CH_2 symmetric stretching corresponding to strong intermolecular interactions. These results strongly revealed that the catalyst can accelerate the dissociation of $Mg(solvents)_x^{2+}$ structure and release a large amount of free Mg^{2+} at the interface. At the same time, the Mg^{2+} migration numbers of different separators were tested and analyzed (Figure 2C; Figure S16, Supporting Information). Compared with the Blank-GF, the ion migration number of MIL101-GF was higher (0.26 vs 0.61), which was attributed to the rapid desolvation ability of MIL101-GF, indicating that MIL101-GF could effectively improve the reaction kinetics of Mg^{2+} migration. Figure 2D and Figure S17 (Supporting Information) graphically describe the above model MIL101-GF catalytic layer promotes the release of Mg^{2+} from the $Mg(solvents)_x^{2+}$ structure and diffuses it to the cathode surface and participating in sulfur/sulfide conversion.

It is well known that the production and movement of soluble MgPSs is one of the main causes of the failure of Mg-S batteries, and the huge dissolution/reaction barrier affects the oxidation reduction transformation kinetics of sulfur migration of the polysulfide migration. As shown in Figure S18A (Supporting Information), MIL-101 (Cr) powder was put into MgPSs solution with the same initial state. After 72 h of reaction, the color of the solution in the bottle was significantly lighter when MIL-101 (Cr) powder was present compared with the blank sample. Since the experimental conditions of the two bottles of solution are exactly the same, the color difference after the reaction can be attributed to the adsorption of MgPSs by MIL-101 (Cr). Figure S18B (Supporting Information) shows the absorption peak near 420 nm in UV-vis spectroscopy to the presence of short chain S_4^{2-}, and the content of short chain S_4^{2-} in MgPSs solution added with MIL-101 (Cr) powder is significantly reduced, the MgPSs in the solution corresponding to MIL-101 (Cr) were reduced to 37.85% of the original content compared with the pure solution, indicating that the MgPSs had a faster conversion in the presence of MIL-101 (Cr) powder, and the S_4^{2-} in the solution was significantly reduced after catalytic conversion.[23] The decrease of polysulfide concentration is caused by the adsorption and reaction of MIL-101 (Cr) powder, which indicates that there is a good chemical interaction between MIL-101 (Cr) powder and MgPSs. Since there is no sulfur present in the MIL-101 (Cr) powder itself, the S-peak in the XPS can be entirely attributable to the adsorbed polysulfide. As shown in Figure S18C (Supporting Information), the peak of S 2p at 164.5 eV can be identified as the peak of MgPSs, while the peak at 161.4 eV can be identified as the peak of MgS, which proves that MIL-101 (Cr) effectively adsorbed MgPSs and promoted its conversion to MgS.[8d] Due to the high chemical activity of MgPSs under open circuit voltage, studying the self-discharge behavior of Mg-S batteries is an effective means to evaluate the ability of the main material to inhibit the shuttle effect. We restart the discharge after maintaining the battery cells 24 h at three distinct states of discharge: 0%, 33%, and 66%, and find that an irreversible capacity decay of the battery with the MIL101-GF much smaller than that with the Blank-GF (Figure S19, Supporting Information). The results indicate that

MIL101-GF can significantly suppress self-discharge behavior by inhibiting the shuttle effect.

To investigate ability of MIL101-GF to catalyze polysulfide conversion electrochemically, we first conducted polysulfide conversion and MgS deposition experiments, and assembled CNT electrode (without sulfur) based symmetric and asymmetric batteries by adding MgS_x to the electrolyte.[24] As shown in Figure 2E, at the sweep speed of 0.2 mV s^{-1}, the cyclic voltammetry (CV) curve based on MIL-101(Cr) symmetric cell easily shows two pairs of redox-polysulfide peaks with larger peak current and area, indicating that more MgPSs are involved in the conversion, while there is almost no obvious peak in the cell with the Carbon.[25] In addition, Figure 2F shows that the cell with MIL-101(Cr) made a rapid response to the formation of MgS within 15 min, which means that MgS_x was quickly converted into MgS deposits with the help of MIL-101(Cr). The cathodes used in both MIL-101(Cr) and Carbon samples are CNT-S.[26] After loading sulfur, it can be seen from Figure S20A (Supporting Information) that there is an obvious CNT structure in the cathode of CNT-S, while it can be seen that the distribution of carbon and sulfur elements is uniform in Figure S20B,C (Supporting Information), which proves that the hot melting method can make elemental sulfur evenly distributed in carbon nanotubes. As shown in Figure S20D (Supporting Information), the characteristic peak of sulfur can be observed in CNT-S, indicating that sulfur has been successfully impregnated into carbon nanotubes. As shown in Figure S20E (Supporting Information), TGA shows that the material has partial decomposition after carbonization, and the sulfur mass content in CNT-S is 75.5%. Rapid ion and electron exchange is also reflected in the results of electrochemical impedance spectroscopy (EIS).[6a] As shown in Figure S21 (Supporting Information), when the battery has just been assembled, both batteries show relatively high internal resistance and diffusion resistance, and cannot show a complete half-arc and diffusion curve, which can be attributed to the existence of passivation layer on the surface of the magnesium anode.[11a] The reason for the large initial resistance of Mg-S battery is mainly caused by the magnesium anode. A passivation layer immediately formed on the surface of magnesium metal upon assembling the cell and the Mg^{2+}-solvents desolvation energy barrier at the anode interface is also high, both of which hinder the transfer of Mg^{2+}. The initial cycle plays an activation role to re-expose the fresh Mg surface. However, if polysulfides are shuttled to the anode surface, the primary passivation layer will be turned into MgS_2/MgS-rich layer, which is then difficult to activate and requires multiple cycles to refresh the Mg surface. The introduction of MIL101-GF can effectively inhibit the shuttle of polysulfides, and thus prevent the formation of MgS_2/MgS passivation layer on the anode, allowing the activation process to occur smoothly. As a result, the resistance drops dramatically, and the magnesium plating/stripping reversibility is also much improved. In order to explore the influence of MIL101-GF on the conductivity, we supplemented the test of ionic conductivity, the ionic conductivity of MIL101-GF is 7 mS cm^{-1}, while the ionic conductivity of Blank-GF is only 3.7 mS cm^{-1}, which indicates that MIL101-GF has high electrical conductivity (Figure S22, Supporting Information). After the first cycle, the cell with MIL101-GF can show a relatively complete half-arc and diffusion curve, and the battery resistance is smaller, and the diffusion slope is larger, indicating that MIL101-GF can effectively accelerate the transfer of electrons and ions. At the sweep speed of 0.05 mV s^{-1}, it can be clearly seen from Figure S23A–C (Supporting Information) that the CV curve of the cell with MIL101-GF has better reversibility. Compared with Blank-GF, cell with MIL101-GF catalyst exhibit smaller peak polarization and larger peak current, thus accelerating polysulfide redox kinetics and improving sulfur utilization. The magnitude of this CV distortion amplifies with increasing scan rates, and Mg-S cell with Blank-GF exhibits significantly more pronounced distortion than Mg-S cell using MIL101-GF. This phenomenon likely stems from the incomplete oxidation of polysulfides at high potential, forming soluble intermediates, resulting in the tailing of the current platform or the broadening of the peak shape, which also indicates that MIL-GF can effectively inhibit the shuttle of polysulfides. The peak current (ip) in Figure S23D,E (Supporting Information) is linear to the square root of the scan rate, and the corresponding slope is summarized in Figure 2G, indicating the typical characteristics of ion diffusion controlled reactions. According to the Randles-Sevcik equation, the Mg^{2+} diffusion coefficient is proportional to the slope, and the slope of the cell with MIL101-GF is significantly higher, indicating that the modified MIL101-GF separator has faster magnesium diffusion transport.[27] In conclusion, it is proved that MIL101-GF has certain catalytic ability in accelerating polysulfide transformation kinetics and the transport rate of Mg^{2+}.

In order to further verify the improvement and practical feasibility of MIL101-GF for the electrochemical performance of Mg-S batteries in actual work, we carried out rate, cycling and high loading tests. As shown in **Figure 3A**, the cell with MIL101-GF delivers outstanding rate performances of 806, 745, 750, 728, and 694 mA h g^{-1} at 0.1, 0.5, 1, 1.5, and 2 C, respectively. When current density being switched back to 0.2 C, the specific capacity also recovers 894 mA h g^{-1}. While the cell with Blank-GF has lower capacity, faster capacity decay, and poor reversibility. Above results indicate that with the help of MIL101-GF, the reaction kinetics of the battery is significantly accelerated, and the reversibility of S/MgS is enhanced. The performance advantages of the cell with MIL101-GF can be seen more clearly in Figure 3B. Figure S24 (Supporting Information) shows the voltage distribution of charge and discharge platforms of the cell with MIL101-GF and Blank-GF at different discharge rates. The cell with MIL101-GF always has a stable discharge voltage platform, while the discharge voltage platforms of cell with Blank-GF disappear when the rate increases to 1.5 and 2 C, which shows that the cell with MIL101-GF has faster conversion dynamics. The slight voltage fluctuations observed during low-rate cycling in Figure S16 (Supporting Information) can be analyzed from two perspectives. At the cathode side, this phenomenon may originate from the incomplete oxidation of dissolved polysulfides at the cathode/electrolyte interface under low current density conditions, which induces repeated transitions between different sulfur redox states and consequently leads to voltage oscillations. At the anode side, the kinetic mismatch between Mg^{2+} deposition/dissolution rates and electrolyte diffusion results in localized current density fluctuations at the Mg metal surface, which are subsequently reflected in the charging voltage profiles. By comparing the charging curves of low rates in Figure S24A,B (Supporting Information), it can be seen that the fluctuation of Blank-GF is more obvious, while that of MIL101-GF

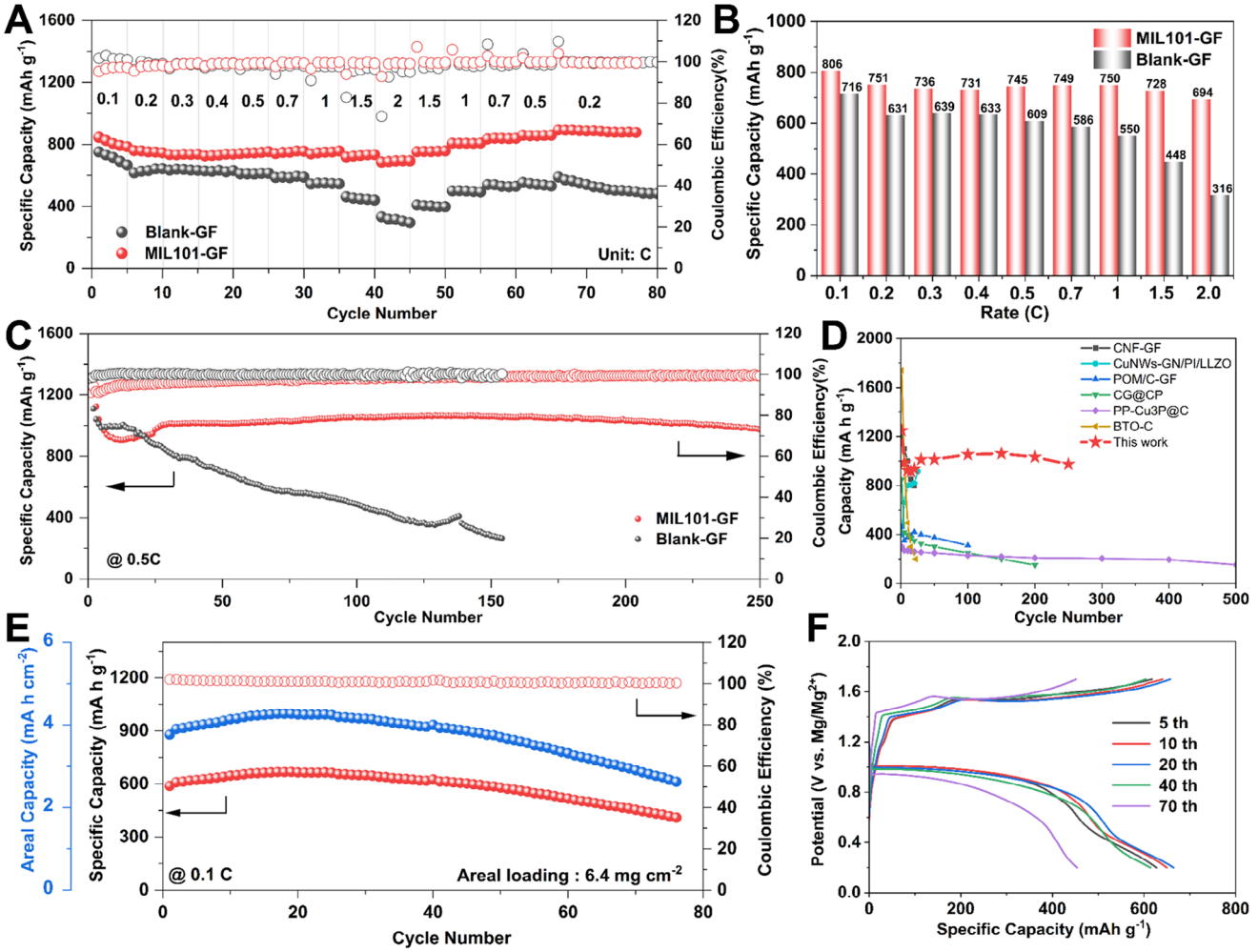

Figure 3. High electrochemical performances of Mg-S cells with MIL101-GF catalyst. A) Rate performance for the cells with Blank-GF and MIL101-GF from 0.05 to 2 C. B) Comparisons of capacity retentions at different current rates. C) Cycling performance of the cells with Blank-GF and MIL101-GF for 400 cycles at 0.5 C. D) Comparison of the electrochemical properties between the MIL101-GF and previously reported separator modified in Mg-S batteries (see Table S1, Supporting Information for details). E) The high mass loading with MIL101-GF cycled at 0.1 C. F) The charge/discharge curve behaviors of the cells with MIL101-GF after different cycles.

is relatively gentle, which once again indicates that MIL101-GF can effectively inhibit the shuttle of polysulfide and benefit uniform magnesium deposition. As shown in Figure 3C, the specific discharge capacity of the cell with MIL101-GF and Blank-GF at 0.5 C occurred some breaks in the early stage, which was mainly caused by the environmental changes in the early stage. The capacity of cell with MIL101-GF hardly decay when the cycling tends to be stable, and even increases slowly in the middle. The specific discharge capacity is stable at ≈1000 mA h g^{-1}, and the specific discharge capacity of 974 mA h g^{-1} can still be maintained after 250 cycles, while the capacity of cell with Blank-GF is only 280 mA h g^{-1} after 150 cycles, intuitively shows that the introduction of MIL101-GF solves the problem of capacity decay in Mg-S batteries. Compared with other similar work related to Mg-S batteries, our work can stably maintain a high specific discharge capacity over a long period of time, with significantly excellent electrochemical performance (Figure 3D). The cells with MIL101-GF have stable voltage platforms in charge/discharge curves with different cycle numbers, which also proves that it can effectively inhibit MgPSs shuttle, thereby helping the sulfur cathode to stabilize its structure (Figure S25).[28] When the Blank-GF is used, the voltage platform is difficult to maintain stability after 100 cycles. In order to further verify the practical feasibility of MIL101-GF, the surface loading of sulfur on the cathode was increased to 6.4 mg cm^{-2}, and the highest discharge capacity of 668 mA h g^{-1} was shown at 0.1 C (Figure 3E). After 70 cycles, the cathode with a high loading can still show the surface capacity of 2.90 mA h cm^{-2}, and the capacity retention rate is 77.0%. It can be seen from Figure 3F, that there is still a stable voltage platform in the charge/discharge curves of different cycle numbers, indicating that the structure is stable and has good reversibility. These results strongly proved that MIL101-GF promoted the transformation kinetics of magnesium ion and polysulfide, improved the utilization of sulfur, and effectively extended the long-lasting life of Mg-S batteries.

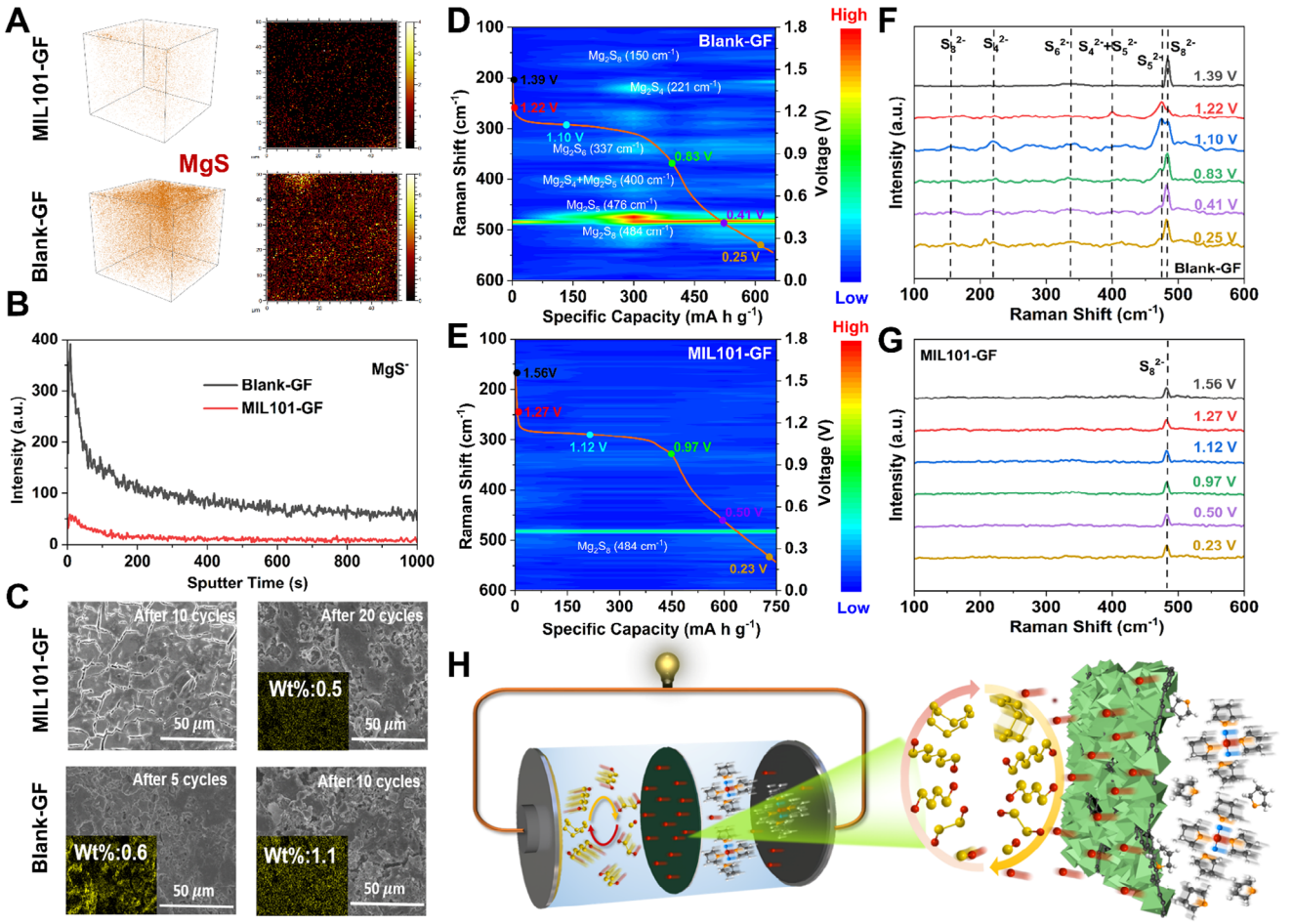

Figure 4. Catalytic mechanism analysis of MIL101-GF after cycling and during discharge process. A) The 3D reconstructions and top-view surface mapping of MgS^- species in cycled with MIL101-GF and Blank-GF after 10 cycles at 0.5 C via TOF-SIMS. B) The signal intensity comparisons of MgS^- species in cycled the cells with Blank-GF and MIL101-GF. C) The morphologies and corresponding mapping of the corresponding Mg anodes after different cycles. D,E) In situ Raman band contours of the Blank-GF and MIL101-GF separators, respectively. F,G) Selected Raman spectroscopy of the Blank-GF and MIL101-GF separators, respectively. H) Illustrated mechanism of the MIL101-GF to achieve fast Mg^{2+} desolvation and accelerate sulfur redox kinetics (the symbols referring to Figure 2A,D).

In order to better understand the catalytic mechanism of MIL101-GF, SEM, and time-of-flight secondary ion mass spectrometry (TOF-SIMS) were performed. Repeated charging and discharging during a long cycle will lead to the generation and deposition of MgS in the cathode. From the TOF-SIMS image (**Figure** 4A) after 10 cycles (under full charge), it could be seen that under the action of MIL101-GF, there was only a small amount of MgS on the top surface of the cathode plate, and almost no MgS in the inside. However, more MgS clusters were found in the cathode corresponding to the Blank-GF, which was due to the presence of dispersed MIL-101 (Cr) in MIL101-GF, could effectively improve the reaction kinetics of MgPSs and reduce the production of "dead sulfur". Therefore, there were only a small number of MgS nanoparticles in the cathode and can be uniformly dispersed, which further confirms the effectiveness of MIL101-GF in homogenizing MgS deposition. As shown in Figure 4B and Figure S26, both the content curve of S^- and the content curve of MgS^- show that the cathode with MIL101-GF is lower, indicating that most of the discharge products are converted into sulfur during the cycling, which realizes the high efficiency and reversibility of the battery.[29] Then the morphology and element distribution of magnesium anode after different cycles were characterized and analyzed (Figure 4C; Figure S27). The surface of the anode in the cell with MIL101-GF is relatively flat, and no obvious uneven deposition occurs even after 20 cycles, and its morphology is even smoother than that of the anode in the cell using Blank-GF after 10 cycles. For the cell with MIL101-GF, the presence of sulfur could not be found after 10 cycles at the anode, indicating that there was very little MgPSs deposited on its surface, and only 0.5% sulfur could be detected after 20 cycles. However, the anode in the cell with Blank-GF showed 0.6% sulfur after 5 cycles, and the content of sulfur deposited after 10 cycles reached 1.1%. The results showed that the presence of MIL101-GF effectively inhibited the shuttle effect of MgPSs and promoted the transformation of MgPSs.[6a]

To further explore the catalytic mechanism of MIL101-GF in the actual work of the battery, in situ Raman spectroscopy test was implemented during discharge process. The structure of

the Mg-S battery is shown in Figure S27, where the light enters the electrode/electrolyte interface from the Mg-anode side.[13c] Figure 4D,F show the in situ time-resolved Raman images of the Mg-S battery based on the Blank-GF separator during the 0.2 C discharge process. The peak at 484 cm^{-1} is attributed to the formation of long chain MgS_8 at the beginning of the discharge, further discharge to 1.22 and 1.1 V, S_4^{2-} + S_5^{2-} and S_4^{2-}, S_6^{2-} corresponding Raman peaks (399 and 220, 338 cm^{-1}) begin to appear, and when the discharge potential reaches 0.83 V or lower, these peaks did not change much, indicating a serious shuttle effect.[7d] In sharp contrast, with the MIL101-GF ion diffusion booster, no other short chain sulfur species was formed on the cathode side during the entire discharge process except for the formation of a peak at 484 cm^{-1} long chain MgS_8 at the beginning of the discharge (Figure 4E,G). These results indicate that MIL101-GF can inhibit MgPSs shuttling and promote the catalytic conversion of MgPSs. The schematic diagram visually illustrates that MIL101-GF with multistage pore structure can effectively catalyze the dissociation of large $Mg(solvents)_x^{2+}$ cluster through pore screening, rapidly form free Mg^{2+} and then further participate in the subsequent sulfur/sulfide conversion (Figure 4H). First, MIL101-GF acts as a physical barrier to MgPSs, inhibiting the shuttle effect to a certain extent. Second, MIL101-GF has electrocatalytic and siphoning functions that release a large amount of free Mg^{2+} through the separator to the cathode/electrolyte surface. Finally, the uniformly dispersed and abundant active sites combined with the fixed MgPSs and a large amount of free Mg^{2+} at the interface for rapid MgPSs conversion, and the uniform conductive structure on MIL101-GF is conducive to rapid electron conduction, which ultimately catalyzes the transformation of sulfur species in Mg-S batteries.

3. Conclusion

In summary, a multistage pore-structured catalytic MIL101-GF was proposed to regulate Mg^{2+} solvation structure, which helps to improve Mg^{2+} diffusion, desolvation, and redox reactions toward high sulfur reaction kinetics. Due to the structure and properties of MIL101-GF, it can effectively promote the release of free Mg^{2+} from the $Mg(solvents)_x^{2+}$ and promote the sulfur redox conversion kinetics. The multistage pore structure of MIL-101 (Cr) and Lewis acid Cr(III) center can effectively adsorb MgPSs and electrocatalyze their conversion. The key role and working mechanism of MIL101-GF in inhibiting polysulfide shuttling, enhancing magnesium ion migration, accelerating desolvation, and catalyzing polysulfide transformation have been investigated by spectroscopical and electrochemical tests, and theoretical simulations. Therefore, the Mg-S cell with the MIL101-GF maintains a high specific discharge capacity of 974 mA h g^{-1} over 250 cycles at 0.5 C and a high rate performance reaches up to 694 mA h g^{-1} at 2 C, which effectively extends the working life of the battery. Furthermore, the cell with a high cathode mass loading of 6.4 mg cm^{-2} delivers a high capacity retention of 77% (the high area capacity of 2.90 mA h cm^{-2}) after 70 cycles at 0.1 C, which provides a reference for the application of MIL101-GF in practical high-performance magnesium sulfur batteries.

Supporting Information

Supporting Information is available from the Wiley Online Library or from the author.

Acknowledgements

The authors acknowledge the National Key R&D Program of China (2021YFA1201503), National Natural Science Foundation of China (Nos. 21972164, 22279161, 12264038, 22309144), China Postdoctoral Science Foundation (Nos. 2024M762318, 2023M731084 and 2023M732561), the Natural Science Foundation of Jiangsu Province (BK. 20210130), the Key R&D Program of Jiangsu Province (BG2024020), Opening funding from Key Laboratory of Engineering Dielectrics and Its Application (Harbin University of Science and Technology) (No. KFM202507, Ministry of Education) as well as the technical support from Nano-X, Suzhou Institute of Nano-tech and Nano-bionics, Chinese Academy of Sciences. Dr. J.W. thanks the funding provided by the Alexander von Humboldt Foundation.

Open access funding enabled and organized by Projekt DEAL.

Conflict of Interest

The authors declare no conflict of interest.

Data Availability Statement

The data that support the findings of this study are available from the corresponding author upon reasonable request.

Keywords

interfacial desolvation, magnesium-sulfur battery, molecular catalysis, pore sieving, sulfur conversion kinetics

Received: March 11, 2025
Revised: April 7, 2025
Published online:

[1] a) Z. W. Seh, Y. Sun, Q. Zhang, Y. Cui, *Chem. Soc. Rev.* **2016**, *45*, 5605; b) R. F. Service, *Science* **2018**, *359*, 1080; c) Y. Liu, M. Zhao, L. P. Hou, Z. Li, C. X. Bi, Z. X. Chen, Q. Cheng, X. Q. Zhang, B. Q. Li, S. Kaskel, J. Q. Huang, *Angew. Chem., Int. Ed. Engl.* **2023**, *62*, 202303363; d) Y. Liang, H. Dong, D. Aurbach, Y. Yao, *Nat. Energy* **2020**, *5*, 646; e) A. Ponrouch, J. Bitenc, R. Dominko, N. Lindahl, P. Johansson, M. R. Palacin, *Energy Storage Mater.* **2019**, *20*, 253; f) B. Scrosati, J. Hassoun, Y.-K. Sun, *Energy Environ. Sci.* **2011**, *4*, 3287.

[2] a) W. Cao, J. Zhang, H. Li, *Energy Storage Mater.* **2020**, *26*, 46; b) Y. Tian, G. Zeng, A. Rutt, T. Shi, H. Kim, J. Wang, J. Koettgen, Y. Sun, B. Ouyang, T. Chen, Z. Lun, Z. Rong, K. Persson, G. Ceder, *Chem. Rev.* **2021**, *121*, 1623; c) X. Liu, Y. Li, X. Xu, L. Zhou, L. Mai, *J. Energy Chem.* **2021**, *61*, 104; d) M. Mao, T. Gao, S. Hou, C. Wang, *Chem. Soc. Rev.* **2018**, *47*, 8804; e) L. Kong, C. Yan, J.-Q. Huang, M.-Q. Zhao, M.-M. Titirici, R. Xiang, Q. Zhang, *Energy Environ. Mater.* **2018**, *1*, 100.

[3] a) D. Aurbach, G. S. Suresh, E. Levi, A. Mitelman, O. Mizrahi, O. Chusid, M. Brunelli, *Adv. Mater.* **2007**, *19*, 4260; b) D. Aurbach, Z. Lu, A. Schechter, Y. Gofer, H. Gizbar, R. Turgeman, Y. Cohen, M. Moshkovich, E. Levi, *Nature* **2000**, *407*, 724; c) H. Fan, Z. Zheng, L. Zhao, W. Li, J. Wang, M. Dai, Y. Zhao, J. Xiao, G. Wang, X. Ding, H. Xiao, J. Li, Y. Wu, Y. Zhang, *Adv. Funct. Mater.* **2019**, *30*, 1909370.

[4] a) M. Hu, G. Li, K. Chen, X. Zhou, C. Li, *Chem. Eng. J.* **2024**, *480*, 148193; b) Y. Zhang, J. Li, W. Zhao, H. Dou, X. Zhao, Y. Liu, B. Zhang, X. Yang, *Adv. Mater.* **2022**, *34*, 2108114; c) X. J. Singyuk Hou, K. Gaskell, P. Wang, L. Wang, J. Xu, R. Sun, C. W. Oleg Borodin, *Science* **2021**, *374*, 172.

[5] a) Q. Pang, X. Liang, C. Y. Kwok, L. F. Nazar, *Nat. Energy* **2016**, *1*, 16132; b) A. Manthiram, Y. Fu, S. H. Chung, C. Zu, Y. S. Su, *Chem. Rev.* **2014**, *114*, 11751; c) H. J. Peng, J. Q. Huang, Q. Zhang, *Chem. Soc. Rev.* **2017**, *46*, 5237.

[6] a) S. Zhang, W. Ren, Y. NuLi, B. Wang, J. Yang, J. Wang, *Chem. Eng. J.* **2022**, *427*, 130902; b) H. Fan, X. Zhang, J. Xiao, Y. Lin, S. Ren, Y. Zhao, H. Yuan, L. Pan, Q. Lin, H. Liu, Y. Su, Y. Su, Y. Liu, Y. Zhang, *Energy Storage Mater.* **2022**, *51*, 873; c) L. Sheng, Z. Hao, J. Feng, W. Du, M. Gong, L. Kang, P. R. Shearing, D. J. L. Brett, Y. Huang, F. R. Wang, *Nano Energy* **2021**, *83*, 105832.

[7] a) X. Yu, A. Manthiram, *ACS Energy Lett.* **2016**, *1*, 431; b) Z. Zhao-Karger, X. Zhao, D. Wang, T. Diemant, R. J. Behm, M. Fichtner, *Adv. Energy Mater* **2015**, *5*, 1401155; c) H. S. Kim, T. S. Arthur, G. D. Allred, J. Zajicek, J. G. Newman, A. E. Rodnyansky, A. G. Oliver, W. C. Boggess, J. Muldoon, *Nat. Commun.* **2011**, *2*, 427; d) B. P. Vinayan, H. Euchner, Z. Zhao-Karger, M. A. Cambaz, Z. Li, T. Diemant, R. J. Behm, A. Gross, M. Fichtner, *J. Mater. Chem. A* **2019**, *7*, 25490.

[8] a) M. Krishna, A. Ghosh, D. Muthuraj, S. Das, S. Mitra, *J Phys. Chem. Lett.* **2022**, *13*, 1337; b) X. Zhou, J. Tian, J. Hu, C. Li, *Adv. Mater.* **2018**, *30*, 1704166; c) H. Du, Z. Zhang, J. He, Z. Cui, J. Chai, J. Ma, Z. Yang, C. Huang, G. Cui, *Small* **2017**, *13*, 1702277; d) L. Wang, P. Jankowski, C. Njel, W. Bauer, Z. Li, Z. Meng, B. Dasari, T. Vegge, J. M. G. Lastra, Z. Zhao-Karger, M. Fichtner, *Adv. Sci.* **2022**, *9*, 2104605.

[9] a) P. Wang, M. R. Buchmeiser, *Adv. Funct. Mater.* **2019**, *29*, 1905248; b) H. Dong, O. Tutusaus, Y. Liang, Y. Zhang, Z. Lebens-Higgins, W. Yang, R. Mohtadi, Y. Yao, *Nat. Energy* **2020**, *5*, 1043; c) J. Zhang, C. You, H. Lin, J. Wang, *Energy Environ. Mater.* **2022**, *5*, 731.

[10] L. Jiang, D. Li, X. Xie, D. Ji, L. Li, L. Li, Z. He, B. Lu, S. Liang, J. Zhou, *Energy Storage Mater.* **2023**, *62*, 102932.

[11] a) Q. Guan, J. Wang, Q. Zhuang, J. Zhang, L. Li, L. Jia, Y. Zhang, H. Hu, H. Hu, S. Cheng, H. Zhang, H. Li, M. Liu, S. Wang, H. Lin, *Energy Environ. Sci.* **2024**, *17*, 3765; b) Y. Han, G. Li, Z. Hu, F. Wang, J. Chu, L. Huang, T. Shi, H. Zhan, Z. Song, *Energy Storage Mater.* **2022**, *46*, 300.

[12] a) X. Song, J. Sun, W. Ren, L. Wang, B. Yang, H. Ning, P. Zhang, Z. Caixiang, Z. Tie, X. Zhang, Y. NuLi, Z. Jin, *Angew. Chem., Int. Ed. Engl.* **2024**, *64*, 202417450; b) J. Xiao, X. Zhang, H. Fan, Y. Zhao, Y. Su, H. Liu, X. Li, Y. Su, H. Yuan, T. Pan, Q. Lin, L. Pan, Y. Zhang, *Adv. Mater.* **2022**, *34*, 2203783; c) C. Li, R. D. Guha, A. Shyamsunder, K. A. Persson, L. F. Nazar, *Energy Environ. Sci.* **2024**, *17*, 190.

[13] a) X. Cheng, Y. Zuo, Y. Zhang, X. Zhao, L. Jia, J. Zhang, X. Li, Z. Wu, J. Wang, H. Lin, *Adv. Sci.* **2024**, *11*, 2401629; b) J. Wang, H. Hu, L. Jia, J. Zhang, Q. Zhuang, L. Li, Y. Zhang, D. Wang, Q. Guan, H. Hu, M. Liu, L. Zhan, H. Adenusi, S. Passerini, H. Lin, *InfoMat* **2024**, *6*, 12558; c) X. Zhang, X. Li, Y. Zhang, X. Li, Q. Guan, J. Wang, Z. Zhuang, Q. Zhuang, X. Cheng, H. Liu, J. Zhang, C. Shen, H. Lin, Y. Wang, L. Zhan, L. Ling, *Adv. Funct. Mater.* **2023**, *33*, 2302624; d) L. Li, H. Tu, J. Wang, M. Wang, W. Li, X. Li, F. Ye, Q. Guan, F. Zhu, Y. Zhang, Y. Hu, C. Yan, H. Lin, M. Liu, *Adv. Funct. Mater.* **2023**, *33*, 2212499; e) J. Wang, J. Zhang, J. Wu, M. Huang, L. Jia, Y. Zhang, L. Li, H. Hu, Q. Guan, F. Liu, M. Liu, H. Lin, H. Adenusi, S. Passerini, *Adv. Mater.* **2023**, *35*, 2302828; f) J. Zhang, L. Pan, L. Jia, J. Dong, C. You, C. Han, N. Tian, X. Cheng, B. Tang, Q. Guan, Y. Zhang, B. Deng, L. Lei, M. Liu, H. Lin, J. Wang, *Nano. Lett.* **2025**, *25*, 3756.

[14] a) Z. Cheng, J. Lian, J. Zhang, S. Xiang, B. Chen, Z. Zhang, *Adv. Sci.* **2024**, *11*, 2404834; b) B. Li, R. Y. C. Wang, S. J. Jingquan Han, C. Z. S. He, *Energy Environ. Sci.* **2024**, *17*, 1854; c) J. E. Zhou, R. C. K. Reddy, A. Zhong, Y. Li, Q. Huang, X. Lin, J. Qian, C. Yang, I. Manke, R. Chen, *Adv. Mater.* **2024**, *36*, 2312471; d) Q. Zhang, S. Jiang, T. Lv, Y. Peng, H. Pang, *Adv. Mater.* **2023**, *35*, 2305532.

[15] H. Yang, Y. Qiao, Z. Chang, P. He, H. Zhou, *Angew. Chem., Int. Ed. Engl.* **2021**, *60*, 17726.

[16] F. Zhang, T. Niu, F. Wu, L. Wu, G. Wang, J. Li, *Electrochimica. Acta.* **2021**, *392*, 139028.

[17] C. Li, X. Zhang, Q. Zhang, Y. Xiao, Y. Fu, H. H. Tan, J. Liu, Y. Wu, *Comput. Theor. Chem.* **2021**, *1196*, 113110.

[18] a) Z. Bai, Z. Wang, T. Wang, Z. Wu, X. Gao, Y. Bai, G. Wang, K. Sun, *Adv. Funct. Mater.* **2024**, *1*, 2419105; b) H. Li, R. Meng, Y. Guo, C. Ye, D. Kong, B. Johannessen, M. Jaroniec, S. Z. Qiao, *Angew. Chem., Int. Ed. Engl.* **2022**, *61*, 202213863; c) L. Wang, W. Hua, X. Wan, Z. Feng, Z. Hu, H. Li, J. Niu, L. Wang, A. Wang, J. Liu, X. Lang, G. Wang, W. Li, Q. H. Yang, W. Wang, *Adv. Mater.* **2022**, *34*, 2110279; d) C. Zhao, Y. Huang, B. Jiang, Z. Chen, X. Yu, X. Sun, H. Zhou, Y. Zhang, N. Zhang, *Adv. Energy Mater.* **2023**, *14*, 2302586.

[19] a) G. Férey, C. Mellot-Draznieks, C. Serre, F. Millange, J. Dutour, S. Surblé, I. Margiolaki, *Science* **2005**, *309*, 2040; b) T. K. Trung, N. A. Ramsahye, P. Trens, N. Tanchoux, C. Serre, F. Fajula, G. Férey, *Microporous Mesoporous Mater.* **2010**, *134*, 134; c) Y. Li, Q. Gao, L. Zhang, Y. Zhou, Y. Zhong, Y. Ying, M. Zhang, C. Huang, Y. Wang, *Dalton Trans.* **2018**, *47*, 6394.

[20] G. Guan, Y. Liu, F. Li, X. Shi, L. Liu, T. Wang, X. Xu, M. Zhao, J. Ding, H. B. Yang, *Adv. Funct. Mater.* **2024**, *34*, 2408111.

[21] Y. Zhou, M. Su, X. Yu, Y. Zhang, J.-G. Wang, X. Ren, R. Cao, W. Xu, D. R. Baer, Y. Du, O. Borodin, Y. Wang, X.-L. Wang, K. Xu, Z. Xu, C. Wang, Z. Zhu, *Nat. Nanotechnol.* **2020**, *15*, 224.

[22] a) Q. Li, G. Liu, Y. Chen, J. Wang, P. Kumar, H. Xie, W. Wahyudi, H. Yu, Z. Wang, Z. Ma, J. Ming, *Adv. Funct. Mater.* **2025**, *1*, 2420327; b) J. Pan, A. P. Charnay, W. Zheng, M. D. Fayer, *J. Am. Chem. Soc.* **2024**, *146*, 35329.

[23] L. Hu, C. Dai, H. Liu, Y. Li, B. Shen, Y. Chen, S.-J. Bao, M. Xu, *Adv. Energy Mater.* **2018**, *8*, 1800709.

[24] R. Zhang, C. Cui, R. Xiao, R. Li, T. Mu, H. Huo, Y. Ma, G. Yin, P. Zuo, *Chem. Eng. J.* **2023**, *451*, 138663.

[25] a) H. Lin, L. Yang, X. Jiang, G. Li, T. Zhang, Q. Yao, G. W. Zheng, J. Y. Lee, *Energy Environ. Sci.* **2017**, *10*, 1476; b) J. Wang, L. Jia, S. Duan, H. Liu, Q. Xiao, T. Li, H. Fan, K. Feng, J. Yang, Q. Wang, M. Liu, J. Zhong, W. Duan, H. Lin, Y. Zhang, *Energy Storage Mater.* **2020**, *28*, 375.

[26] S. Cheng, J. Wang, S. Duan, J. Zhang, Q. Wang, Y. Zhang, L. Li, H. Liu, Q. Xiao, H. Lin, *Chem. Eng. J.* **2021**, *417*, 128172.

[27] X. Li, Q. Guan, Z. Zhuang, Y. Zhang, Y. Lin, J. Wang, C. Shen, H. Lin, Y. Wang, L. Zhan, L. Ling, *ACS Nano* **2023**, *2*, 1653.

[28] Y. Ji, X. Liu-Théato, Y. Xiu, S. Indris, C. Njel, J. Maibach, H. Ehrenberg, M. Fichtner, Z. Zhao-Karger, *Adv. Funct. Mater.* **2021**, *31*, 2100868.

[29] a) R. Fang, H. Xu, B. Xu, X. Li, Y. Li, J. B. Goodenough, *Adv. Funct. Mater.* **2020**, *31*, 2001812; b) C. Zhao, A. Daali, I. Hwang, T. Li, X. Huang, D. Robertson, Z. Yang, S. Trask, W. Xu, C. J. Sun, G. L. Xu, K. Amine, *Angew. Chem., Int. Ed. Engl.* **2022**, *61*, 202203466.